



# 1 Impacts from cascading multi-hazards using hypergraphs: a case 2 study from the 2015 Gorkha earthquake in Nepal

3

4 Alexandre Dunant<sup>1\*</sup>, Tom R. Robinson<sup>2</sup>, Alexander L. Densmore<sup>1</sup>, Nick J. Rosser<sup>1</sup>, Ragindra Man Rajbhandari<sup>3</sup>, Mark  
5 Kinsey<sup>4</sup>, Sihan Li<sup>5</sup>, Prem Raj Awasthi<sup>3</sup>, Max Van Wyk de Vries<sup>6,7</sup>, Ramesh Guragain<sup>8</sup>, Erin Harvey<sup>1</sup> and Simon Dadson<sup>9</sup>

6

7 <sup>1</sup> Institute of Hazard, Risk, and Resilience and Department of Geography, Durham University, Durham, UK

8 <sup>2</sup> School of Earth and Environment, University of Canterbury, Christchurch, New Zealand

9 <sup>3</sup> UN Resident Coordinator's Office, Nepal

10 <sup>4</sup> School of Geography, Politics, and Sociology, Newcastle University, Newcastle, UK

11 <sup>5</sup> Department of Geography, University of Sheffield, Sheffield, UK

12 <sup>6</sup> Department of Geography, University of Cambridge, Cambridge CB2 3EL, UK

13 <sup>7</sup> Department of Earth Sciences, University of Cambridge, Cambridge CB3 0EZ, UK

14 <sup>8</sup> National Society for Earthquake Technology-Nepal (NSET), Nepal

15 <sup>9</sup> School of Geography and the Environment, University of Oxford, UK

16

17

18 \* Corresponding author: [alexandre.dunant@durham.ac.uk](mailto:alexandre.dunant@durham.ac.uk)

19

20

## 21 Abstract

22 This study introduces a new approach to multi-hazard risk assessment, leveraging hypergraph theory to model the  
23 interconnected risks posed by cascading natural hazards. Traditional single-hazard risk models fail to account for the  
24 complex interrelationships and compounding effects of multiple simultaneous or sequential hazards. By conceptualising  
25 risks within a hypergraph framework, our model overcomes these limitations, enabling efficient simulation of  
26 multi-hazard interactions and their impacts on infrastructure. We apply this model to the 2015  $M_w$  7.8 Gorkha  
27 earthquake in Nepal as a case study, demonstrating its ability to simulate the primary and secondary effects of the  
28 earthquake on buildings and roads across the whole earthquake-affected area. The model predicts the overall pattern of  
29 earthquake-induced building damage and landslide impacts, albeit with a tendency towards over-prediction. Our  
30 findings underscore the potential of the hypergraph approach for multi-hazard risk assessment, offering advances in  
31 rapid computation and scenario exploration for cascading geo-hazards. This approach could provide valuable insights  
32 for disaster risk reduction and humanitarian contingency planning, where anticipation of large-scale trends is often more  
33 important than prediction of detailed impacts.

34

## 35 Keywords

36 Cascading multi-hazards, multi-hazard modelling, earthquake impacts, landslides, Nepal, network modelling,  
37 hypergraphs



38 **1. Introduction**

39

40 There is a growing recognition over the last 15 years that natural hazards can interact and occur in conjunction with  
41 each other, leading to a potential compounding effect that is greater than the sum of the single-hazard impacts (Kappes  
42 et al., 2012; Terzi et al., 2019). While the global prevalence of cascading hazards specifically is difficult to quantify  
43 reliably, there are increasing calls for effective multi-hazard risk assessments (e.g., Ward et al., 2022). Multi-hazards are  
44 defined by UNISDR (2016) as "events [that] may occur simultaneously, cascadingly or cumulatively over time, and  
45 taking into account the potential interrelated effects". Multi-hazard approaches seek to overcome the limitations of a  
46 narrower focus on single-hazard models, which are unable to account for the observed inter-relationships between  
47 different hazards as well as potential compounding or cascading effects (e.g., Gill and Malamud, 2014; Tilloy et al.,  
48 2019; Dunant, 2021; Ming et al., 2022). Multi-hazard approaches to risk are now widely encouraged (e.g., UNISDR,  
49 2005; Government Office for Science, 2012) and are increasingly integrated into risk assessment (see recent reviews by  
50 Gill et al., 2022; Ward et al., 2022).

51

52 There remain, however, some important challenges and limitations with multi-hazard risk assessment. Because of the  
53 difficulties in recognising, understanding, and defining the inter-relationships between hazards, and the lack of data on  
54 their co-dependence (Tilloy et al., 2019; Hochrainer-Stigler et al., 2023), most 'multi-hazard risk' models simply  
55 overlay single hazards without considering their interactions – an approach that Gill and Malamud (2014) termed  
56 'multi-layer single hazard'. Even when hazard-hazard interactions are considered in risk models, there is still a lack of  
57 comprehensive approaches that capture the intricate interplay among hazards, exposure, and vulnerability beyond  
58 simple spatial overlaps (Mignan et al., 2014; de Ruiter et al., 2020). These interactions are critical because of the  
59 possibility that risks may be clustered in space and time or may amplify each other, as demonstrated by Mignan et al.  
60 (2014). Zschau (2017) extended the ideas of Gill and Malamud (2014) to risk assessment, distinguishing between risk  
61 from single hazards, risk from multi-layer single hazards, and risk from multi-hazards – the latter allowing for dynamic  
62 hazard interactions, but no dynamic interactions between hazard and exposure or vulnerability). Hochrainer-Stigler et  
63 al. (2023) noted that hazard-exposure relationships and changes in exposure over time, as well as vulnerability, are also  
64 critical to fully characterise multi-risks. This complexity means that multi-hazard risk modelling can be both  
65 computationally expensive and extremely demanding of quality input data (e.g., Kappes et al. 2012). Multi-hazard risk  
66 models may also be limited by the diversity of hazard types that can be incorporated, mismatches in the appropriate  
67 spatial and temporal scale of analyses, and complex data requirements (e.g., Kappes et al., 2012; Tilloy et al., 2019;  
68 Dunant, 2021).

69

70 A further complication is the growing need for national, regional, or even global-scale risk assessments, in order to  
71 understand potential patterns of impacts, provide science-based evidence for disaster risk reduction and advocacy, and  
72 allow coordinated planning (see review by Ward et al., 2020). At the same time, data are available at ever-increasing  
73 spatial and temporal resolution, including information on populations, building stock, and topography, as well as  
74 datasets on hazard drivers such as rainfall forecasts or observed precipitation. While these are welcome developments,  
75 the combination of demands for increasing scale and increasingly-fine spatial and temporal resolution data leads to a  
76 much higher computational burden. Addressing the need for both larger spatial scales and finer spatio-temporal  
77 resolutions is a growing challenge for the assessment of multi-hazard risks. The distribution of risk may also be highly  
78 spatially imbalanced if exposed elements are concentrated in specific areas, meaning that grid-based or GIS-based  
79 approaches to risk modelling may expend much computational effort on areas where risk is low or negligible.



80

81 To address these concerns, Dunant et al. (2021a) proposed a novel approach to multi-hazard risk modelling using graph  
82 theory. In this framework, both the hazards and the elements at risk are modelled as a set of interconnections between  
83 nodes. For example, a house can be linked to ground accelerations in an earthquake, or a hillslope to rainfall in a storm.  
84 This framework can then be used to generate many disaster scenarios by cascading from node to node according to a set  
85 of rules (e.g., a threshold earthquake shaking value for slope failure). The resulting network model is highly  
86 computationally efficient, and the network structure is a natural fit to the simulation of coincident or cascading events  
87 and their propagation through exposure networks (Dunant et al., 2021a) because network structures are purposefully  
88 designed to capture the interdependencies and feedbacks among different elements. The framework is agnostic to the  
89 types of objects that can be included, so it can be easily adapted to include hazard-hazard, hazard-exposure, and  
90 hazard-vulnerability relationships. It is also highly flexible, so that the links between objects can be represented via  
91 different interactions depending on the level of understanding and data availability, including threshold values,  
92 empirical functions, fuzzy distributions, process models, or other approaches (e.g., Tilloy et al., 2019).

93

94 Despite its advantages, however, the network model suffers from some important limitations. Most critically, because  
95 the interactions in a network model are modelled as pairs, the computational burden grows substantially as the number  
96 of components (nodes and edges) of the model increases. Prior applications focused on the epicentral area of the 2016  
97  $M_w$  7.8 Kaikōura earthquake (Dunant et al., 2021a) and the area around Franz Josef township (Dunant et al., 2021b),  
98 both in New Zealand and containing on the order of hundreds of nodes. Expanding the network model to a national  
99 scale at a similar resolution would increase the model size by several orders of magnitude. Similarly, increasing the  
100 number of hazards that are considered would lead to a combinatorial increase in interactions and rapid growth in  
101 computation time.

102

103 Here we propose a new approach to modelling the impacts of multi-hazards using hypergraphs – two-dimensional  
104 surface equivalents of the pairwise links found in the graph-theory network model of Dunant et al. (2021a). The  
105 hypergraph model retains the advantages of the network approach while simultaneously reducing the model complexity.  
106 Below, we first present a brief review of graphs and hypergraphs and outline the benefits of using hypergraphs in a  
107 multi-hazard risk modelling framework. We describe the structure of the multi-hazard impact model, including its  
108 components and the interactions between nodes. We illustrate its application by simulating the impacts from the 2015  
109  $M_w$  7.8 Gorkha earthquake in Nepal, as an exemplar of a large-scale event that had cascading effects on people and  
110 infrastructure due to both primary and secondary hazards. We close by considering wider potential applications of the  
111 hypergraph model, including national- or regional-scale disaster scenario ensembles and how they might be used to  
112 support humanitarian contingency planning (e.g., Robinson et al., 2018).

113

## 114 **2. Summary of graph and hypergraph approaches**

115

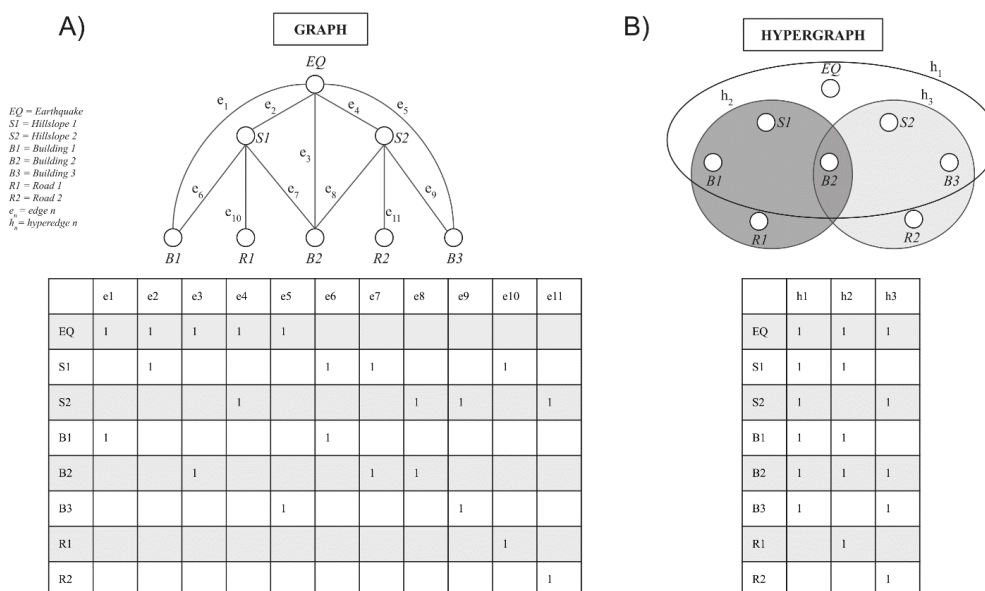
116 A graph is essentially a mathematical representation of a network. The term was originally introduced by Sylvester  
117 (1878) but graph theory had been used more than a hundred years before by Euler (1736) to solve the Seven Bridges of  
118 Königsberg problem. Since then, graph theory has been used in a wide variety of fields such as geography, computer  
119 science, social science, and biology (e.g., Buzna et al., 2006; Chorley & Kennedy, 1971; Dezső & Barabási, 2002;  
120 Dorogovtsev & Mendes, 2003).

121



122 A graph comprises a set of nodes connected by edges. In the context of risks posed by environmental hazards, such  
 123 nodes may represent a geographical location (spatially explicit; e.g., a fault segment, or a house) or a nominal property  
 124 (spatially implicit; e.g., the occurrence of an earthquake) and the edges represent the relations between the nodes (e.g.,  
 125 earthquake shaking affecting exposed houses) (Fig. 1A).

126



127

128 **Figure 1: Graph (A) and hypergraph (B) representations of a hypothetical set of hazard and exposure interactions. The same**  
 129 **set of elements are represented in both graphical form (top) and tabular form as incidence matrices (bottom). In the tables, a**  
 130 **blank cell means no interaction between the nodes, and a value of 1 means that interactions are possible between the nodes.**

131

132 A defining characteristic of graphs is the set of pairwise connections or edges between nodes that define the  
 133 relationships between these nodes. For example, we would represent earthquake shaking on a set of hillslopes as edges  
 134 between the earthquake and each hillslope that is affected. In tabular form, each edge is represented by a row in a  
 135 relational database, called an incidence matrix (Fig. 1A). The edges are directional, so a two-way relationship – for  
 136 example, a hillslope potentially affecting a road via landslides, and a road potentially affecting a hillslope via excavation  
 137 and steepening – would be represented by two separate rows.

138

139 As summarised by Dunant et al. (2021a), here we consider relationships between nodes that are observed or felt – that  
 140 is, via shaking, mass movement, or water flow. We also consider that nodes are connected if (1) the geographical effect  
 141 of one node overlaps that of another, and (2) that effect is relevant to considering impacts from hazards. For example,  
 142 earthquake ground shaking might affect a hillslope and trigger a new landslide or the mobilisation of loose material in a  
 143 debris flow; to allow for these effects, we would represent the relationship between earthquake and the hillslope as an  
 144 edge, and the relationship between the hillslope and any houses or road segments on it as a series of additional edges  
 145 (Fig. 1A). If we were to assume that the earthquake ground motion can potentially cause direct impacts on houses but  
 146 not roads, then the earthquake would be connected to the houses by edges but not to the road segments (Fig. 1A).

147



148 In contrast, a hypergraph is a special type of graph where the edges, called hyperedges, can link one or more nodes (Fig.  
149 1B). This allows us to represent interactions that extend beyond a single pair of nodes (Wolf et al., 2016). Compared to  
150 pairwise edges, which only connect two nodes, hyperedges can connect multiple nodes and provide a more natural  
151 representation for the spatial overlap between exposed elements, like houses, and geographical hazard footprints.  
152 Hyperedges can thus represent nested information between the nodes of the system, such as their properties or locations,  
153 with far fewer tabular entries (Fig. 1B). The hypergraph uses fewer edges to represent the same number of interactions  
154 for a given number of nodes; this size difference (e.g., for the example in Figure 1,  $11 \times 8 = 88$  entries for the graph  
155 framework and  $3 \times 8 = 24$  for the hypergraph framework) highlights the efficiency of the hypergraph approach.

156

157 The increased efficiency enabled by hypergraphs becomes more apparent when dealing with large, interconnected  
158 datasets and when iterative data manipulation is required. For example, we can run hundreds or thousands of separate  
159 simulations on the same hypergraph, choosing different events or altering input parameters within a Monte Carlo  
160 framework (e.g., Dunant et al., 2021a) to generate ensemble distributions of scenario outcomes (Robinson et al., 2018).  
161 The improvement in computation time allows the hypergraph framework to be applied to multi-hazards risk assessment  
162 over larger extents, over longer time periods, and with more complex interactions than would be feasible using a  
163 GIS-based approach or standard graph framework.

164

### 165 3. Methodology

166

167 Below we describe the setup and operation of the multi-hazard hypergraph model and describe its application to the  
168 2015 Gorkha earthquake.

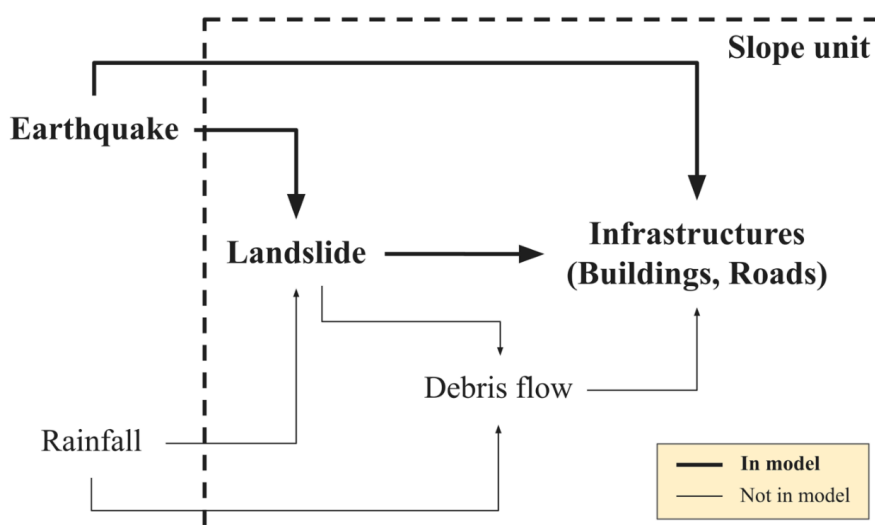
169

#### 170 3.1 Model overview and setup

171

172 The model is based around a set of interactions between elements in Nepal that are drawn from experience in both the  
173 annual monsoon (Kincey et al., 2022; Jimée et al., 2019; Goda et al., 2015; Rosser et al., 2021; Kargel et al., 2016) and  
174 recent earthquakes, including the 2015 Gorkha event (e.g., Roback et al., 2018; Milledge et al., 2019; Kincey et al.,  
175 2021). For the simulations in this paper, the model is driven only by earthquakes (Fig. 2) and seeks to assess the risk to  
176 buildings and roads at a national scale. Earthquake shaking is simulated as a spatial distribution of peak ground  
177 acceleration (PGA) values; these could be derived from measurements or generated for a potential scenario earthquake  
178 via a shaking model. For the experiments shown here, we use empirical PGA values estimated by the US Geological  
179 Survey Shakemap for the 2015 Gorkha earthquake  
180 (<https://earthquake.usgs.gov/earthquakes/eventpage/us20002926/shakemap/pga>). Earthquake shaking can affect  
181 infrastructure either directly (described via a set of fragility functions) or by triggering landslides. Landslides, in turn,  
182 may affect both buildings and roads. In this version of the model, other hazards such as rainfall and floods are not  
183 considered, but they could be added via additional sets of hyperedges and interactions.

184



185

186 **Figure 2: Driving stimuli and important process interactions for the area affected by the 2015 Gorkha earthquake in Nepal.**

187 **The elements that are included in the multi-hazard impact experiments documented here are shown in bold text.**

188

189 To model coseismic landslides, we subdivide the landscape into discrete units and consider the characteristics of the  
 190 topography as well as the driving mechanisms within those subdivisions. Here we divide the landscape into slope units  
 191 that are bounded by drainages and divide lines (Alvioli et al., 2016; Woodard et al., 2024) (see Supplemental  
 192 Information and Fig. S1). Woodard et al. (2024) demonstrated that slope units are preferable to gridded topography  
 193 when representing landslide susceptibility, especially for input landslide data that are imprecise or highly spatially  
 194 variable in quality.

195

196 The hyperedges are constructed based on the interactions in Figure 2. A hyperedge connects the earthquake node with  
 197 all of the slope units and buildings within the ‘footprint’ of the earthquake, defined by the extent of a minimum PGA (X  
 198 g) contour. Similarly, hyperedges connect each slope unit with the buildings and roads (divided into 100 m segments)  
 199 within it; we therefore assume that landslides from one slope unit cannot impact elements in another. Attributes for each  
 200 building, road segment, and slope unit, such as location, PGA, building type, landslide susceptibility, are stored on the  
 201 hyperedges and can be displayed as continuous values in a tabular form. We describe each of these attributes below.

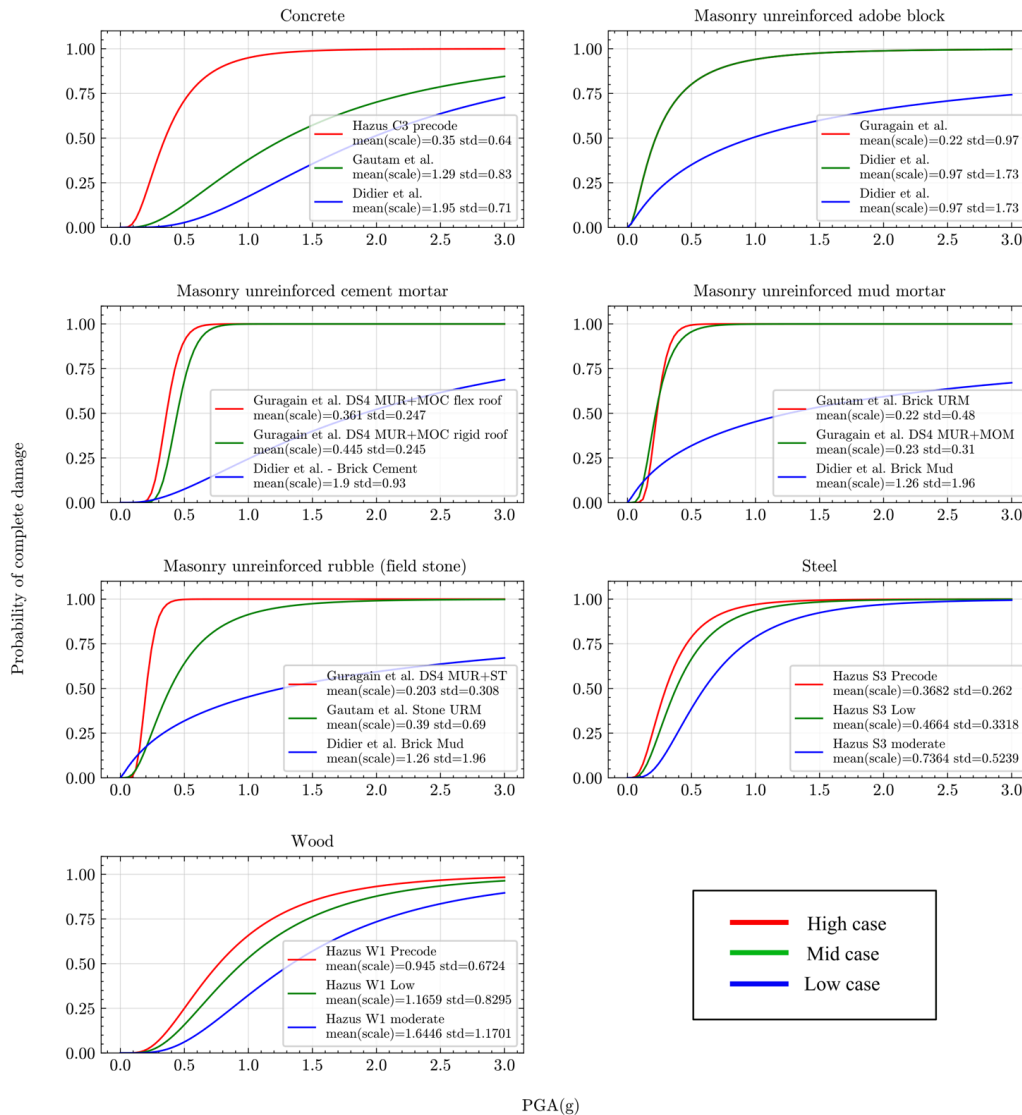
202

203 We use building locations and roads taken from the Humanitarian OpenStreetMap Team, covering the whole of Nepal,  
 204 and available at [https://data.humdata.org/dataset/hotosm\\_npl\\_buildings](https://data.humdata.org/dataset/hotosm_npl_buildings) and  
 205 [https://data.humdata.org/dataset/hotosm\\_npl\\_roads](https://data.humdata.org/dataset/hotosm_npl_roads), respectively (accessed 1 January 2021). The datasets contain c. 7.1  
 206 million building polygons and c. 3 million road segments. Because we lack specific information on the construction  
 207 type of each building to assess its fragility, we instead use exposure data from the Modeling Exposure Through Earth  
 208 Observation Routines (METEOR) project (<https://maps.meteor-project.org/map/building-exposure-map-of-nepal>)  
 209 (version 2020-02-15), which includes a list of building types and the number and value of each type within each cell of  
 210 a 90 x 90 m grid across Nepal. The PGA value of the 2015 Gorkha earthquake is extracted at the centroid of each  
 211 METEOR grid cell. To account for variability in construction detail and quality within these broad types, we adopt low,



212 middle, and high fragility functions for the ‘complete damage’ state for typical building types in Nepal from the  
 213 METEOR dataset (Fig. 3). We take the definition of ‘complete damage’ from the Hazus framework of the US Federal  
 214 Emergency Management Agency (FEMA, 2020). We generate a weighted-average fragility function for the buildings  
 215 within each 90 x 90 m grid cell based on the proportion of different building types; thus, in the absence of any  
 216 national-scale building-specific information, all buildings within that cell are assumed to have the same average  
 217 fragility. We assess the likelihood of ‘complete damage’ because this implies loss of usability or habitability, with  
 218 consequences for displacement and disruption to life and livelihoods, and is typically used to estimate fatality and injury  
 219 rates (FEMA, 2020).

220



221

PGA(g)



222 **Figure 3: Fragility functions used in the hypergraph network modelling.** Each panel shows fragility curves for a different  
223 building type in the METEOR dataset, and which relate the peak ground acceleration (PGA, in g) to the probability of being  
224 reduced to a complete damage state. Note that each sigmoidal fragility curve is defined by two parameters: a mean or scale  
225 parameter that sets the PGA value for a 50% probability of complete damage, and a standard deviation (std) that defines the  
226 spread of the curve. Parameter values and sources for the fragility curves are included in the plots.

227

228 We estimate landslide susceptibility based on topographic factors alone, using a seven-parameter static susceptibility  
229 model that incorporates elevation, hillslope aspect, distance to rivers, plan-view curvature, regional relief, local hillslope  
230 gradient, and a terrain ruggedness index. These factors are derived from a 10 m digital elevation model (DEM) that was  
231 downsampled from the 5 m Advanced Land Observing Satellite World 3D DEM  
232 (<https://www.aw3d.jp/en/products/standard/>). We generate the susceptibility model using a gradient boosting machine  
233 learning approach, XGBoost, implemented in Python. For the experiments shown here, the susceptibility model is  
234 trained on the locations of coseismic landslides triggered by the 2015 Gorkha earthquake as mapped by Kinsey et al.  
235 (2021), yielding an area under the receiver operating characteristic (ROC) curve of 0.75 (Fig. S2). We stress that this  
236 susceptibility layer is used simply as an exemplar which is optimised for the 2015 Gorkha earthquake; for other model  
237 applications, susceptibility data generated with other approaches (see review in Reichenbach et al., 2018), or trained on  
238 different inventories, could be substituted. Because landslide susceptibility is modelled on a 10 x 10 m grid, each slope  
239 unit contains a unique distribution of cell-wise susceptibility values in the range [0,1], and each building polygon or  
240 road segment overlaps with one or more cellwise susceptibility values. Importantly, because the multi-hazard model is  
241 intended to simulate dynamic cascading scenarios, we choose not to include earthquake shaking as a determining factor  
242 in the static landslide susceptibility model. This choice preserves independence between shaking, landslide triggering,  
243 and the propagation of hazards along the hyperedges within the model.

244

245 We extract the mean and standard deviation of susceptibility for each slope unit, building and road segment, although  
246 other measures of the distribution could also be used. Because we lack general building or road fragility functions for  
247 landslides that are comparable to those for earthquakes and that encompass the wide range of possible landslide types  
248 and sizes (see Luo et al., 2023, for a recent review), we adopt a simplified binary vulnerability model, such that any  
249 building or road that is affected by a landslide is considered as 'impacted'.

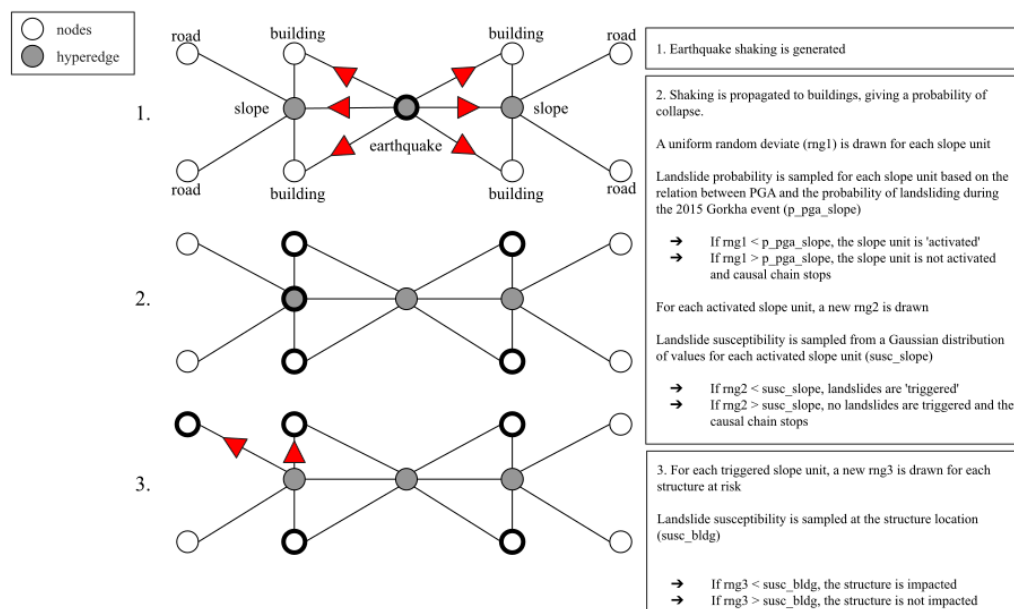
250

### 251 **3.2 Simulation steps**

252

253 In each simulation, the model works iteratively through the hyperedges that connect the driving stimulus of earthquake  
254 shaking to the other elements in the model, checking against a condition to see whether that hyperedge of the network is  
255 'activated' – i.e., a building is damaged by earthquake shaking, or a slope unit is affected by one or more landslides.  
256 Activation of that hyperedge then allows the stimulus to propagate, and potentially to cascade along other hyperedges if  
257 further conditions are met (Fig. 4). The simulation continues until all cascades stop and no further impacts are possible.

258



259

260 Figure 4. Step-by-step overview of the hypergraph framework for modelling cascading multi-hazard impacts. The  
 261 hypergraph is represented in a simplified example on the left and the algorithm steps are specified on the right. The  
 262 simplified hypergraph assumes a landscape with two slope units, each of which contains two buildings and two road  
 263 segments. The causal cascades of the algorithm are represented in three steps; from top to bottom, these are (1) earthquake  
 264 shaking, (2) tests for ‘activation’ of a hillslope and ‘triggering’ of landslides, and (3) tests for impacts on structures by  
 265 landslides. In the simplified hypergraph, black outlines show the hyperedges where hazards occur (e.g., landslides are  
 266 triggered by the earthquake), and the nodes that are damaged by either shaking (step 2) or landsliding (step 3). The process is  
 267 embedded in an iterative Monte Carlo simulation to determine the uncertainty associated with each step, creating a series of  
 268 disaster scenarios that can be queried for further analysis.

269

270 In the experiments shown here, the first step is to work through the hyperedge that connects the earthquake to the  
 271 individual buildings to assess their damage state. For each building, we assign the PGA value at the centroid of its 90 x  
 272 90 m METEOR grid cell. We use the high, middle, and low weighted mean fragility functions for that grid cell to  
 273 determine the likelihood of that building being completely damaged – which is equivalent to the proportion of buildings  
 274 within that 90 x 90 m grid cell in the METEOR dataset that is completely damaged. This likelihood of complete damage  
 275 [0,1], reproduces the weighted mean fragility when applied over the METEOR grid cell. The low, middle, and high  
 276 cases provide a range of outcomes for an individual building at a specific PGA value. The per-building likelihoods of  
 277 complete damage under the three cases can then be summed by slope unit or administrative area to give the total  
 278 predicted number of completely-damaged buildings in each area.

279

280 Next, we assess which slope units are ‘activated’ by ground shaking (Fig. 4). Activation of a slope unit means that the  
 281 ground accelerations are high enough to potentially trigger one or more landslides, if this is permitted by the  
 282 topographic conditions as represented by the landslide susceptibility. Again, this allows the stimulus to propagate within  
 283 the earthquake hyperedge to the slope unit, and potentially to cascade within that slope unit (and affect buildings or road  
 284 segments within it). In these experiments, we conduct a logistic regression between PGA and the locations of landslides  
 285 in the inventory of coseismic landslides triggered by the 2015 Gorkha earthquake (Kinney et al., 2021) to define the



286 regional-scale probability of landslide occurrence as a lognormal function of PGA (see Supplemental Information and  
287 Fig. S3). We calculate the mean PGA value within each slope unit, and use that to determine the corresponding  
288 probability of landsliding within the slope unit from the lognormal function. That probability, in turn, is compared with  
289 a uniform random deviate to determine whether each slope unit is activated or not. Thus, over large numbers of  
290 simulations, slope units with more observed coseismic landslides will be activated more frequently, but the exact pattern  
291 of activations in each individual simulation – and thus the portion of the hypergraph network that is sampled – will vary.  
292

293 For all slope units that are activated, the model proceeds to subsequent hyperedges to assess whether buildings or road  
294 segments are affected by direct landslide occurrence (Fig. 4). In the experiments shown here, this is a two-step process.  
295 We first check if a landslide occurred within the slope unit. Even if the shaking was strong enough to potentially trigger  
296 a landslide (i.e., the slope unit was ‘activated’), it might still have a low likelihood of experiencing landsliding due to  
297 low susceptibility (i.e., it was not ‘triggered’). Triggering in the slope unit is determined by drawing a value (A) from a  
298 Gaussian distribution of landslide susceptibility with the same mean and standard deviation as the distribution of  
299 susceptibility values in that slope unit, and comparing that value with a uniform random deviate (B). We employ a  
300 Gaussian distribution for efficiency, as this can be calculated in advance of the simulation, and note that it provides a  
301 reasonable fit to the actual distribution across a wide range of slope units (Supplemental Information, Fig. S4). If the  
302 susceptibility value A is smaller than B, then no landslide has occurred in that slope unit, and propagation along that  
303 hyperedge stops. If A is larger than B, then one or more landslides has occurred in that slope unit. We then check if each  
304 building and road segment within the slope unit is affected by this landsliding by comparing the landslide susceptibility  
305 value at the infrastructure location with another uniform random deviate. If the random deviate exceeds the landslide  
306 susceptibility value, then the building or road segment remains unaffected by the landslide (in other words, even if a  
307 landslide happens in the slope unit, it doesn’t affect the building or road). Then, the simulation continues to evaluate  
308 other buildings or roads within the same slope unit, and then moves on to other slope units activated by the earthquake.  
309 If the random deviate is less than the susceptibility value, then the building or road segment is impacted by landsliding.  
310 In this case, we add it to the pool of affected elements for this simulation and move to the next building or road. We  
311 continue this process to search iteratively through all slope units in the network to generate a single cascading impact  
312 scenario.

313

### 314 3.3 Outputs and evaluation

315

316 The iterative simulation process outlined above is repeated within a Monte Carlo framework to create an ensemble of  
317 scenarios, each of which explores a different set of outcomes within the same set of hyperedges. In the experiments  
318 shown here, we generate 10,000 scenarios from the initial stimulus of the 2015 Gorkha earthquake. Hence, all scenarios  
319 in these experiments use the same spatial distribution of PGA values and thus the probability of an individual building  
320 suffering complete damage by shaking stays the same. What differs between scenarios are the details of which slope  
321 units are activated, which slope units experience landsliding, and which buildings or road segments are impacted by  
322 those landslides. Thus, we take the likelihood of a structure being affected by landsliding over the whole ensemble as  
323 the proportion of the 10,000 scenarios in which the structure is impacted. This leads to a shaking impact likelihood and  
324 a landslide impact likelihood, both in the range [0,1], for each of the buildings and road segments in our combined  
325 dataset.

326



327 To explore the trade-off between spatial resolution and model performance, we aggregate the structure-level results over  
328 successively larger administrative units. Nepal is divided, from smallest unit to largest, into 6,743 wards, 753 urban and  
329 rural municipalities, 77 districts, and 7 provinces. Aggregation across these units allows us to evaluate the performance  
330 of the model against independent measures of earthquake impacts from the 2015 Gorkha earthquake at different spatial  
331 resolutions. For buildings damaged by earthquake shaking, we evaluate the model in two ways. First, we sum up the  
332 per-building likelihoods of complete damage in each district for the low, middle, and high fragility estimates – which  
333 yields the number of completely-damaged buildings in each case – and compare those sums to incident reports  
334 summarising the number of "fully damaged" buildings per district and published on the Government of Nepal's Bipad  
335 Portal (<http://drrportal.gov.np/> – see also Chaulagain et al., 2018) based on the Post-Disaster Damage and Needs  
336 Assessment (PDNA) (National Planning Commission, 2015). This assesses the ability of the model to estimate the  
337 absolute number of damaged buildings. While this data remains the most extensive for validation purpose, the PDNA  
338 was done urgently after the disaster with limited systematic gathering hence it relies on judgement by the PDNA  
339 participants and, therefore, carry significant uncertainty (Lallemand et al., 2017). Note that wards and municipalities  
340 were defined in the federal restructuring of Nepal in 2017, and so data on damaged buildings from the 2015 earthquake  
341 are not available at ward or municipality level. Second, we take the mean likelihood of complete damage in each  
342 district, in the range [0,1], and compare that with the presence or absence of damaged buildings in each of the 77  
343 districts. This second measure is independent of the absolute number of buildings, and gives information instead on the  
344 ability of the model to anticipate the occurrence of one or more completely damaged buildings in an area.

345

346 For structures impacted by landslides, we derive similar statistical measures for model evaluation. First, we sum up the  
347 per-structure likelihoods of landslide impact over successively larger areas of aggregation – ward, municipality, district,  
348 and province. Because there are no systematic published data on observed landslide impacts on buildings and roads in  
349 the 2015 earthquake, we generate an estimate of affected structures by overlaying the coseismic landslide polygons  
350 from Kincey et al. (2021) on our building and road dataset; all structures that intersect with a mapped landslide polygon  
351 are assumed to have been impacted by landsliding in the earthquake. Note that this measure of landslide impacts does  
352 not consider the significant post-earthquake changes in landslide footprint and debris runout (e.g., Tian et al., 2020;  
353 Kincey et al., 2022). Also, the coseismic landslides were mapped on medium-resolution satellite imagery (c. 10 m,  
354 equivalent to our DEM and derived topographic metrics) and so will have omitted small landslides or rockfalls,  
355 especially in areas of dense vegetation or steep topography (e.g., Williams et al., 2018); this error and the inherent  
356 uncertainty in mapped landslide outlines (Kincey et al., 2021) mean that our estimate of the number of  
357 landslide-affected structures is likely to represent a lower bound. We then sum the observed number of impacted  
358 buildings and road segments by administrative area to compare with our modelled totals. We also compare the mean  
359 likelihood of landslide impact, averaged by administrative area and ranging from [0,1], with the presence or absence of  
360 landslide impacts in that area. We evaluate the relationship between these parameters with the area under the ROC  
361 curve and the F1 score.

362

## 363 4. Results

364

### 365 4.1 Impacts from earthquake shaking

366

367 We first consider modelled impacts from earthquake shaking alone. Unsurprisingly, the probability of complete damage  
368 per building, or equivalently the proportion of completely-damaged buildings within each 90 x 90 m exposure grid cell,

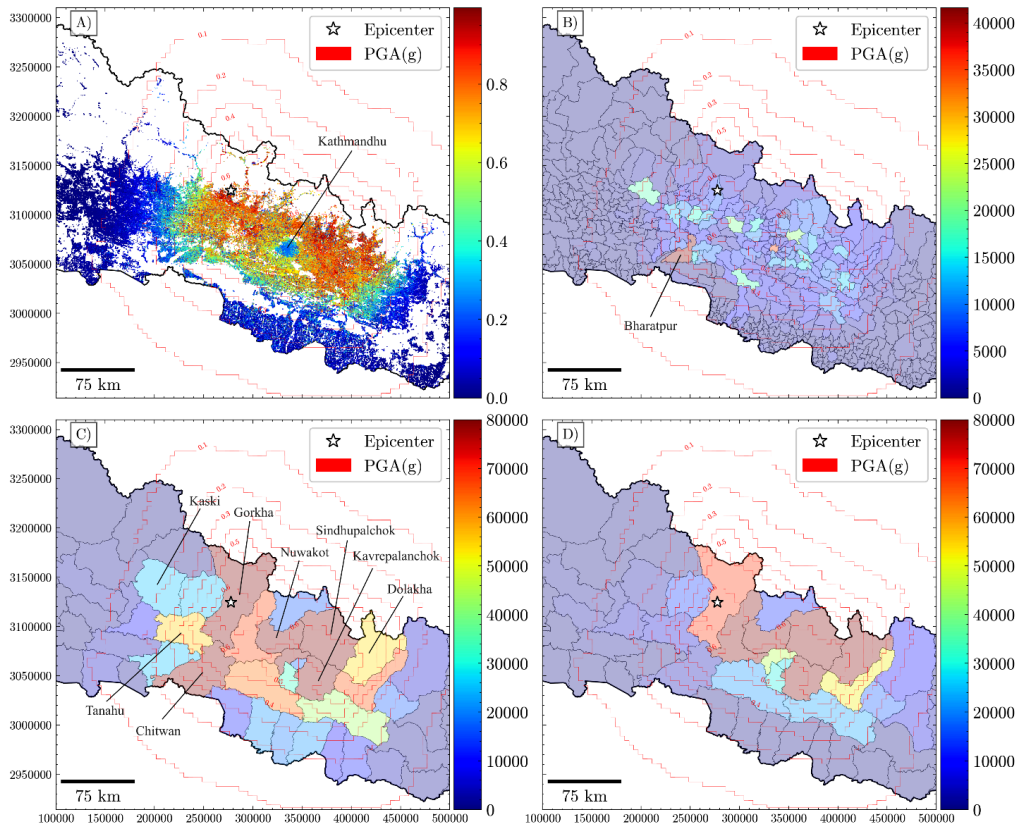


369 closely matches the estimated PGA contours from the Gorkha earthquake (Fig. 5A). There are particularly high  
370 probabilities in the hill and mountain districts, especially to the east and northeast of Kathmandu, where the values  
371 exceed 0.7. Notably, these values generally increase to the north and this increase is cut off only by the lack of buildings  
372 above elevations of around 3,500 m in northern Nepal (visible as the white areas in Fig. 5A). The Kathmandu Valley  
373 itself yields a low proportion of completely-damaged buildings, despite moderately high PGA values, due to the  
374 preponderance of less-fragile building types.

375

376 We convert the proportion of completely-damaged buildings per grid cell into a sum total aggregated over  
377 municipalities (Fig. 5B) and districts (Fig. 5C). These totals reflect the PGA pattern and the weighted mean fragility  
378 functions, but importantly also the number of buildings within each administrative area. When aggregated by  
379 municipality, the largest modelled totals tend to occur in the more densely-populated Middle Hills in the vicinity of  
380 Kathmandu, rather than the more sparsely-populated north. There are some notable exceptions to this pattern, such as  
381 Bharatpur to the south of the earthquake epicentre (Fig. 5B), which combines a large stock of fragile building types with  
382 moderately high PGA values. When aggregated by district, the largest modelled totals are again dominated by areas  
383 with both large numbers of buildings and moderate to high PGA values (Fig. 5C). With the exception of Chitwan to the  
384 south of the epicentre, the largest totals are found in districts where PGA exceeded 0.4 g. It is instructive to compare the  
385 aggregated pattern by district to the actual numbers of completely-damaged buildings (Fig. 5D). There are broad  
386 similarities between modelled and observed totals, especially in the hill and mountain districts of Sindhupalchok,  
387 Nuwakot, and Kavrepalanchok. Notably, the model over-predicts the impacts in districts close to the epicentre,  
388 including Gorkha and Chitwan, and under-predicts the impacts at the eastern margin of the rupture in Dolakha (Fig.  
389 5D).

390



391

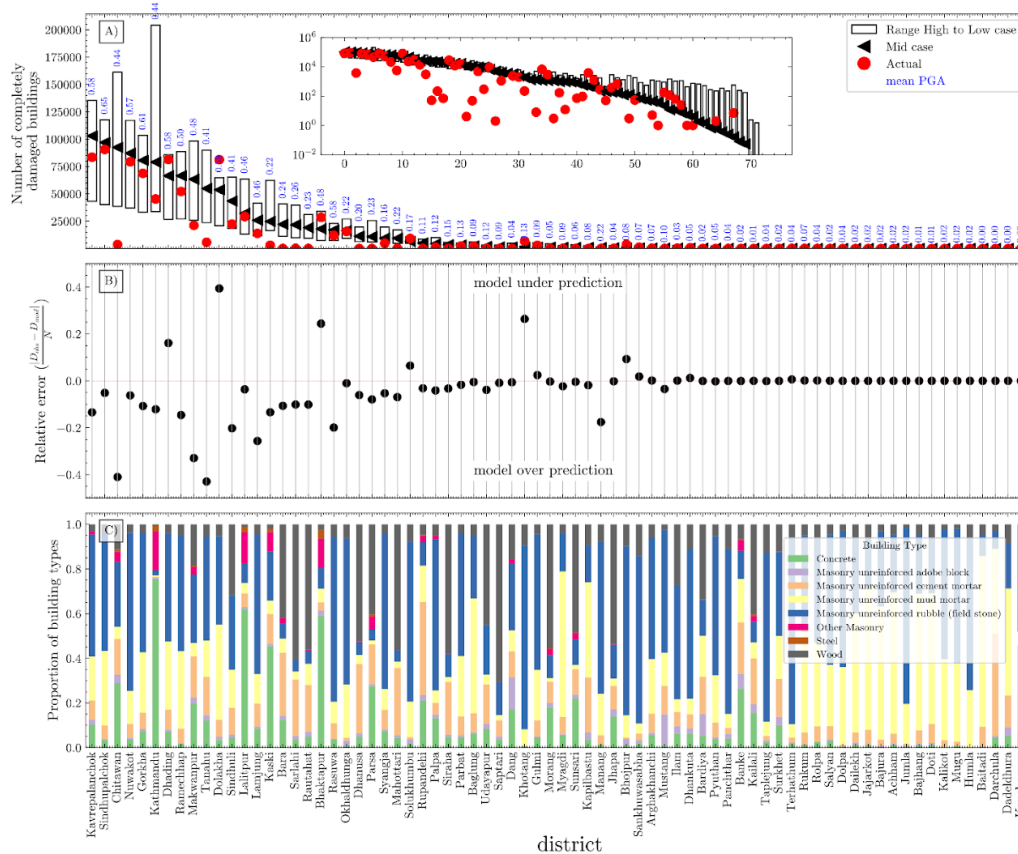
392 Figure 5: Modelled building impacts from shaking in the 2015 Gorkha earthquake. In all panels, the red contours show the  
393 estimated PGA values from the earthquake in g. Note that these results are derived from the middle-case fragility functions in  
394 Fig. 4. A, modelled probability of complete damage for individual buildings across the country. This is equivalent to the  
395 proportion of completely-damaged buildings in each 90 x 90 m grid cell in the METEOR exposure dataset. B, modelled sum  
396 total of completely-damaged buildings aggregated by municipality. C, modelled sum total of completely-damaged buildings  
397 aggregated by district. D, actual sum of reported “fully damaged” buildings aggregated by district. Note similar colour scales  
398 in panels C and D.

399

400 To better visualise the agreement between modelled and observed totals of completely-damaged buildings, we compare  
401 the observed totals for all 77 districts in Nepal with model results using the high, middle, and low fragility cases (Fig.  
402 6A). For most districts with non-zero impacts, the observed totals fall within the range of model results using the  
403 different fragility curves, with a slight bias toward model over-prediction (Fig. 6B). Among the top 15 districts in terms  
404 of modelled impacts, observed impacts fall below that range in three districts (Chitwan, Tanahu, and Kaski; see Fig. 5C  
405 for locations), within that range in 11, and above that range in only one (Dolakha). Alternatively, out of the ‘14  
406 worst-affected districts’ identified by the Government of Nepal, observed impacts fall within the range of model results  
407 in thirteen districts, with Dolakha being the only outlier. The model thus appears to be somewhat conservative in that it  
408 slightly over-predicts building impacts due to shaking in the 2015 earthquake. The mismatch between modelled and  
409 observed totals is not clearly related to building typologies (Fig. 6C). There may be a weak correlation with shaking;



410 districts with significant over-prediction tend to be those with lower mean PGA values (typically <0.44 g) while  
411 Dolakha has a larger mean PGA (0.59 g), and we explore this point in the Discussion.  
412



413  
414 Figure 6: A, comparison of modelled and observed numbers of completely-damaged buildings per district in the 2015 Gorkha  
415 earthquake. Bars show the range of modelled results for each district using high and low fragility cases (see Fig. 4), with the  
416 middle case shown by the black arrow. Red dots show the reported numbers of "fully damaged" buildings. Blue numbers  
417 show the mean PGA for each district, in g. The inset shows the same quantities with a logarithmic y-axis scale. B, mismatch  
418 between observed ( $D_{obs}$ ) and modelled ( $D_{mod}$ ) numbers for each district, normalised by the total number of buildings in that  
419 district ( $N$ ). Negative values indicate model over-prediction, while positive values indicate model under-prediction. Note that  
420 impacts in most of the districts with non-zero damage values are slightly under-predicted. C, proportion of different building  
421 types in each district from the METEOR exposure data set. There is no clear correlation between the residuals in panel B and  
422 the dominant building types.

423

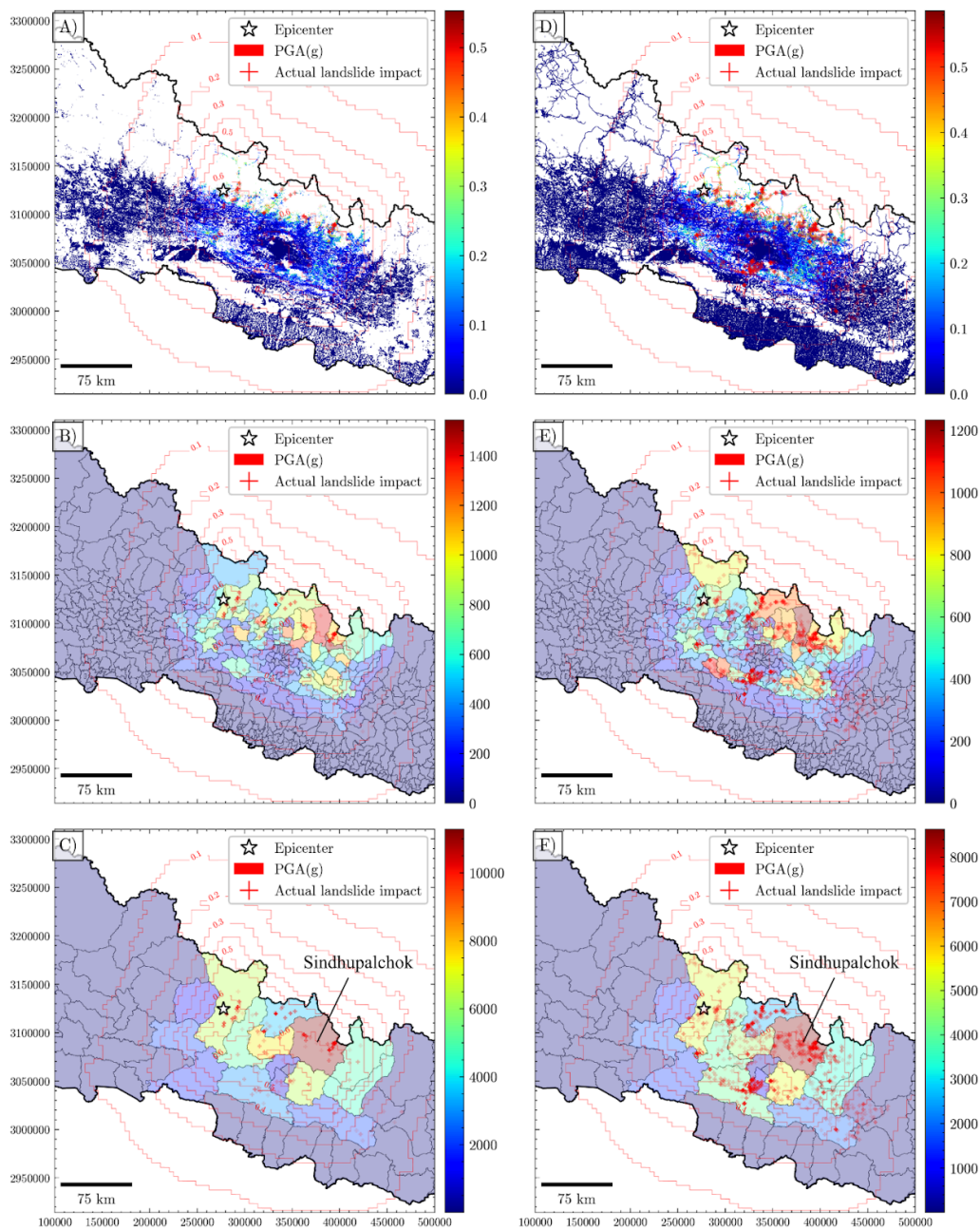
#### 424 4.2 Impacts from coseismic landslides

425

426 As with shaking damage, the modelled probability of a building (Fig. 7A) or road segment (Fig. 7D) being impacted by  
427 a coseismic landslide scales with PGA; this is simply a consequence of the assumed relationship between PGA and  
428 landslide triggering (Fig. S3). Higher probability values are found in northern areas of Nepal, where landslide



429 susceptibility is elevated (Fig. S2). We aggregate these probabilities to estimate the number of impacted buildings and  
430 road segments at the municipality (Fig. 7B, E) and district (Fig. 7C, F) levels. The regions experiencing the highest  
431 predicted impacts closely align with those observed, notably concentrated in Sindhupalchok district, where both  
432 modelled and observed landslide impacts are most prevalent (Fig. 7C, F). Again, these areas predominantly lie in  
433 northern Nepal where susceptibility to landslides is greatest, contrasting somewhat with the distribution of modelled  
434 shaking damage. This disparity may stem from the higher and more widely dispersed density of buildings in the  
435 southern regions. Consequently, while shaking-related damage appears diffuse, landslide-related damage is more  
436 focused in specific regions due to localized exposure. Importantly, the model anticipates approximately an order of  
437 magnitude fewer building impacts from landslides as compared to those damaged by shaking (note the scale difference  
438 between Figs. 5 and 7). We also note that, while the overall spatial patterns of modelled building and road impacts are  
439 similar, the model predicts somewhat higher numbers of road impacts (by about 50%), and that this generally matches  
440 the observed differences in intersections between these infrastructure types with coseismic landslides (Fig. 7). Roads are  
441 typically sited along or near valley floors, thus increasing their exposure to landslides. Additionally, there is a  
442 significant association between roads and landslides (e.g., Hearn and Shakya, 2017; McAdoo et al., 2018), suggesting  
443 that the interaction between landslides and roads may cover a broader spatial extent compared to the relationship  
444 between landslides and buildings.  
445



446



447 **Figure 7: Modelled structural impacts from coseismic landslides in the 2015 Gorkha earthquake. In all panels, the red**  
448 **contours show the estimated PGA values from the earthquake in g. The red crosses show observed landslide impacts on**  
449 **buildings (left column) and road segments (right column), derived by mapping the intersections between those structure**  
450 **locations and the coseismic landslide inventory of Kincey et al. (2021). A, modelled probability of impact for individual**  
451 **buildings across the country. B, sum of per-building probabilities aggregated by municipality, of which there are 753 in**  
452 **Nepal. C, sum of per-building probabilities aggregated by district, of which there are 77 in Nepal. D, modelled probability of**  
453 **impact for individual 100 m road segments across the country. E, sum of per-road segment probabilities aggregated by**  
454 **municipality. F, sum of per-road segment probabilities aggregated by district.**

455

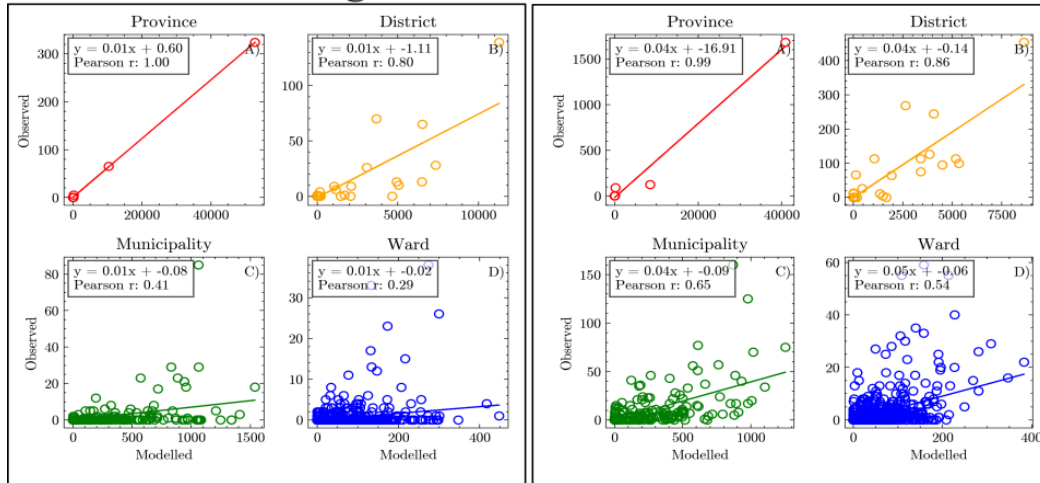
456 The correlation between the modelled and observed numbers of buildings impacted by landslides depends upon the area  
457 over which they are aggregated (Fig. 8). At province ( $n = 7$ ) and district ( $n = 77$ ) levels, there is an approximately linear  
458 relationship between modelled and observed numbers of buildings, with a Pearson's correlation coefficient  $>0.80$  (Fig.  
459 8). At municipality and ward levels, however, the correlation is much weaker. Notably, modelled numbers of buildings  
460 over-predict the observed totals by a factor of about 50-100, irrespective of the administrative area. Similar results are  
461 seen for road segments: good linear correlations for province- and district-level aggregation, much weaker performance  
462 for municipalities and wards, and over-prediction of impacts by a factor of about 20-25 (Fig. 8).

463



## Buildings

## Roads

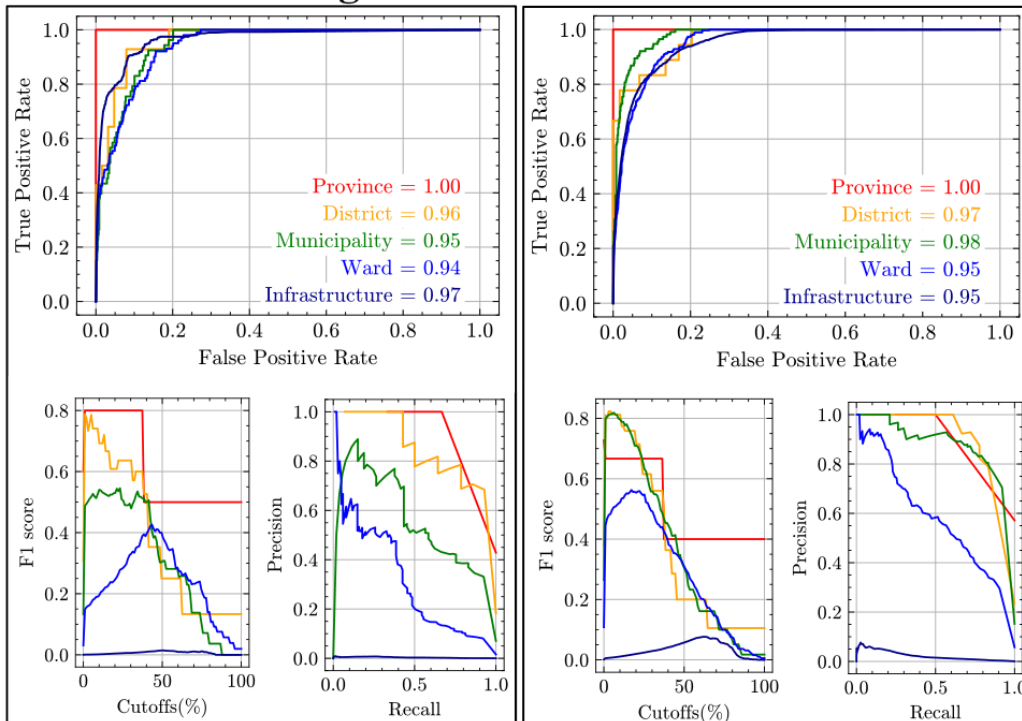


464

465 Figure 8: Comparison of modelled (x-axis) and observed (y-axis) numbers of building and road impacts from coseismic  
466 landslides in the 2015 Gorkha earthquake, summed over different administrative areas. Straight lines show best-fit linear  
467 regression results. Note differences in axis limits depending on the area of aggregation by province (red), district (orange),  
468 municipality (green), or ward (blue).

## Buildings

## Roads



469



470 **Figure 9: ROC (top), F1 (lower left), and precision-recall (lower right) curves for coseismic landslide impacts of buildings and**  
471 **road segments aggregated over province, district, municipality, ward and at the individual infrastructure scale. Numbers in**  
472 **the top panels show the area under the ROC curves. Line colours match the symbol colours in Fig. 8.**

473

474 As a more permissive test of the model's ability to anticipate landslide impacts, we also compare the mean likelihood of  
475 landslide impacts, averaged by administrative area, with the presence or absence of impacts in those areas. While the  
476 area under the ROC curves is high for all aggregation levels (Fig. 9), this is likely due to the strong imbalance between  
477 prediction categories (i.e., there are many more non-impacted buildings than impacted buildings, so the ROC curve is  
478 dominated by the large number of true negative model results). In contrast, precision-recall curves show a progressive  
479 decrease in model performance at progressively smaller levels of aggregation, from province to ward, and very low  
480 precision at the scale of an individual building or road segment (Fig. 9). Because F1 scores combine precision and  
481 recall, they show a similar pattern (Fig. 9); across the full range of thresholds, F1 scores for both buildings and roads  
482 (Fig. 9) are highest for province- and district-level aggregation and lowest for ward-level aggregation. For an optimal  
483 model threshold, province-level aggregation achieves maximum F1 scores of around c. 0.8 for buildings and c. 0.65 for  
484 roads. The maximum F1 scores for buildings are also around 0.8 for districts and diminish progressively to 0.55 for  
485 municipalities and 0.4 for wards. For roads, the maximum F1 scores are 0.8 for districts and municipalities, and 0.55 for  
486 wards. In sum, these results indicate that, while the model can reproduce the spatial pattern of landslide impacts at the  
487 provincial or district scale, its predictive capability is much weaker when assessing impacts within smaller  
488 administrative units like municipalities and wards, and it should not be used to predict impacts to individual buildings or  
489 road segments.

490

## 491 **5. Discussion**

492

### 493 **5.1 General observations**

494

495 Overall, the hyperedge model is able to reproduce the overall spatial pattern of the impacts from the Gorkha earthquake.  
496 This lends some confidence that the model framework could be adapted to estimate the potential impacts from a future  
497 event, such as a large earthquake or rainstorm. While the computational efficiency of the hyperedge approach is a  
498 notable strength – enabling rapid simulations involving extensive elements, such as the approximately 7.1 million  
499 individual buildings and 3 million road segments in our case – its significance extends beyond speed and flexibility  
500 because it fosters the generation of multi-hazard scenario ensembles, diverging from the limitation of focusing solely on  
501 deterministic impact scenarios. Robinson et al. (2018) demonstrated the advantages of scenario ensembles over the  
502 more common approach of single deterministic scenarios, especially as a tool for facilitating awareness of what could  
503 be possible in a future event. While creation of multi-hazard scenario ensembles is our wider goal, the experiments  
504 shown here focus on multiple realisations of the same past event for the purpose of evaluation.

505

506 A key finding of the experiments is the trade-off between model performance, in terms of the ability to anticipate both  
507 the spatial pattern and number of impacts, and the resolution of the model outputs. Because of the probabilistic nature of  
508 the model and limitations in our understanding of exposure, earthquake shaking, and landslide susceptibilities, we  
509 cannot say with confidence which buildings were impacted by hazards related to the 2015 earthquake. As we aggregate  
510 the model results over increasingly large areas, however, our ability to rank those areas in terms of impact, and to  
511 estimate the number of structures affected, increases monotonically. While our results can therefore not be used to



512 anticipate the risk to individual households, they could be used by organisations working at a larger scale to identify  
513 areas that are more or less prone to different types of hazards, and provide a relative ranking in terms of the number and  
514 scale of expected impacts. Thus, the value and potential usefulness of the hypergraph approach as implemented here lies  
515 more in informing planning over larger spatial scales, at which the model performs best, as opposed to rapid response to  
516 a particular event where detailed spatial information would be required. There is some indication that absolute numbers  
517 of affected structures could be generated for larger administrative units by extrapolating the scaling by our analysis of  
518 the 2015 earthquake (see, for example, Fig. 8), but we hesitate to draw conclusions from a single earthquake without  
519 further testing.

520

## 521 5.2 Over-prediction and relative impacts between hazards

522

523 We note that the model over-predicts the number of impacts at all levels of aggregation, and is therefore conservative in  
524 terms of anticipating the scale of impacts for the 2015 earthquake. The possible reasons for this over-prediction are  
525 likely to differ for shaking and landslide impacts. The mismatch in the number of buildings damaged by shaking is  
526 especially notable for districts with moderate mean PGA values (typically  $<0.5$  g; Fig. 6A). The sigmoidal fragility  
527 functions used in the model are steepest at moderate PGA values (Fig. 3); for the middle case, this corresponds to PGA  
528 values of  $\sim 0.2$ - $0.5$  g for the most common building types in Nepal. Thus, small uncertainties in PGA will yield large  
529 differences in the likelihood of complete damage, and thus in the numbers of completely-damaged buildings in our  
530 model experiments. This issue is compounded by the highly-uncertain values of ground motion in the Gorkha  
531 earthquake stemming from the paucity of strong-motion recordings, as noted by Goda et al. (2015). We also note that  
532 our experiments do not account for aftershocks, including the  $M_w$  7.3 earthquake that occurred on 12 May and that  
533 ruptured the eastern end of the 25 April slip patch under Dolakha district (Avouac et al., 2015). This event likely led to  
534 additional building damage which was included in the observations but is not simulated here, perhaps leading to  
535 under-prediction in Dolakha in particular.

536

537 Over-prediction of observed landslide impacts, in contrast, may result from a range of different factors. As noted above,  
538 in the absence of an independent dataset of landslide impacts on buildings or roads in the 2015 earthquake, we have  
539 generated these data by intersecting those elements at risk with the coseismic landslide inventory of Kincey et al.  
540 (2021). This is likely to underpredict the actual number of impacts due to errors and limitations in landslide mapping as  
541 well as the potential for buildings to be omitted from the Humanitarian OpenStreetMap database. It is also important to  
542 note that our approach relies on a probabilistic sampling of an underlying landslide susceptibility dataset in order to  
543 anticipate (1) the slope units in which a landslide is most likely to be triggered, and (2) the buildings and road segments  
544 that were most likely to be affected. Our results are thus highly dependent upon the quality of the underlying  
545 susceptibility information. In the experiments described here, susceptibility is a static quantity that depends only upon  
546 local topography. Because we are focused on a single event, there is no direct provision for dynamic variation in  
547 susceptibility over time or for other factors that may affect landslide occurrence, such as the presence or absence of  
548 antecedent rainfall, soil moisture or other measures of ground condition, or land cover. Further applications of the  
549 model could incorporate susceptibility estimates that are trained on other landslide inventories – for example,  
550 time-varying susceptibility that captures the evolution of landslide hazard over time (e.g., Tian et al., 2020; Kincey et  
551 al., 2021, 2022) or that depends upon other causative factors (e.g., Reichenbach et al., 2018).

552



553 Our model result that the number of buildings damaged by ground shaking is approximately an order of magnitude  
554 greater than that impacted by landslides is difficult to test directly because of the lack of a systematic description of the  
555 sources of building damage in the 2015 Gorkha earthquake. It is broadly consistent, however, with previous work on the  
556 relative importance of secondary hazards – including landslides – and ground shaking in determining earthquake losses.  
557 Bird and Bommer (2004) assessed the relative impacts of ground shaking and ground failure on direct and indirect  
558 losses in earthquakes. They found that fatal landslides occurred in 10 of their 50 studied earthquakes and that landslides  
559 could be the primary cause of building damage in affected areas, locally overshadowing ground shaking. Overall,  
560 however, ground shaking was the primary cause of building damage in 88% of their studied earthquakes, and landslides  
561 in only 6%. They also found that landslide-induced disruption of road or transport networks was much more common  
562 than building damage, which matches our model results for the Gorkha earthquake. Daniell et al. (2017) argued that  
563 ground shaking has caused 62% of total economic costs in earthquakes over the period 1900-2016, with landslides  
564 responsible for 5% of total costs. Marano et al. (2010) found that 21.5% of the fatal earthquakes in the PAGER-CAT  
565 database had deaths due to secondary hazards, but that these were rarely the main cause of death. Landslides were the  
566 leading cause of non-shaking-related deaths if the 2004 Great Sumatra earthquake was excluded, although they  
567 accounted for about an order of magnitude fewer deaths than ground shaking. In contrast, Budimir et al. (2014)  
568 demonstrated that earthquakes with landslides typically cause more fatalities than those without, independent of other  
569 factors such as earthquake size or affected population. Their results demonstrate the need to account for the full  
570 multi-hazard cascade in anticipating losses at anything other than a simplified regional scale (e.g., Bird and Bommer,  
571 2004; Daniell et al., 2017).

572

### 573 5.3 Limitations

574

575 While the model operates on a hyperedge that connects every structure within the dataset, there are a number of factors  
576 that cannot be resolved at a building scale. Notably, PGA values were gridded at a spatial resolution of 100 by 100 m,  
577 meaning that we have no information on the actual accelerations experienced by individual buildings or road segments.  
578 Similarly, while landslide susceptibility was estimated using a comparatively fine-scale DEM with a grid size of 10 x 10  
579 m, each individual building or road segment occupies at most a few grid cells and the susceptibility values are thus  
580 highly location-dependent. It is also important to note that we do not simulate the triggering, occurrence, and runout of  
581 individual landslides, nor do we ‘place’ landslides in the landscape as would be done for example in a landscape  
582 evolution model (e.g., Croissant et al., 2017; 2019). Such a calculation would dramatically increase both the model  
583 complexity, making it infeasible to construct a multi-hazard scenario ensemble at a national scale. Because of this  
584 limitation, we cannot directly evaluate which elements at risk are directly impacted by landslides, nor can we anticipate  
585 which elements may be affected by remobilisation and runout of landslide debris (e.g., Kincey et al., 2022). By  
586 sampling the landslide susceptibility distribution for each slope unit, and the landslide susceptibility values for each  
587 building, we are (over enough iterations) recovering those distributions, but we cannot overcome the inherent  
588 uncertainty in susceptibility at those locations. Finally, the METEOR exposure dataset contains information on the  
589 building types and numbers within each 90 x 90 m grid cell, but we have no information on the type and fragility of  
590 individual buildings. Therefore, while impact likelihood is calculated at the scale of individual structures, we stress that  
591 this estimate is only meaningful across the whole scenario ensemble, and should never be interpreted as a statement that  
592 ‘building X will be affected by this earthquake’.

593



#### 594 **5.4 Other applications**

595

596 Because of its efficiency, the framework allows exploration of other elements of model performance, including the  
597 distinction between false positive and false negative errors. While performance measures such as the area under an  
598 ROC or precision-recall curve can be used to define an ‘optimum’ model outcome, the model application and users may  
599 determine which type of error is more important to minimise. For example, a humanitarian organisation may view false  
600 positives as more acceptable than false negatives; the former may lead at worst to unnecessary preparations, whereas  
601 the latter means that impacts are not anticipated and may delay relief and recovery efforts. By quickly generating  
602 numerous multi-hazard scenarios, the framework can be run with users to explore these different outcomes, and to  
603 examine the specificity of model results to the details of a particular scenario (e.g., Robinson et al., 2018). The model  
604 could also be used to explore ‘what-if’ questions with users to examine the effects of particular interventions or  
605 remediation measures. In addition, the efficiency of the framework could be used to explore the evolution of risk over  
606 time, where increased simulation length or time resolution would lead to an increase in computational cost. Thus, the  
607 effects of policy decisions, climate change and consequent changes in hazard occurrence, or demographic shifts on the  
608 pattern of anticipated impacts could be explored (Zschau, 2017).

609

610 The flexibility of the hyperedge framework also lends itself to other types of simulation. Other elements of the  
611 multi-hazard chain shown in Fig. 2 could be included; for example, susceptibility to landslide debris remobilisation and  
612 runout could be included and sampled for each element at risk, allowing the model to anticipate both the direct impacts  
613 within an event as well as potential longer-term impacts arising from later secondary hazards (e.g., Fan et al., 2019;  
614 Kincey et al., 2022). Impacts from other types of driving events, such as monsoon rainfall, could also be explored. It  
615 would be feasible, for example, to generate an ensemble of scenarios around different rainfall patterns associated with a  
616 seasonal monsoon outlook, or with different iterations of shorter-term weather forecasts, to look at the pattern and  
617 specificity of impacts. Such an application would be subject to the comparatively low spatial resolution of both  
618 observational (e.g., Hou et al., 2014) and forecast rainfall data products, so that – just as with the earthquake scenarios  
619 developed here – the impact results at the scale of an individual structure would not be meaningful. The hyperedge  
620 framework would, however, allow exploration of the trade-offs between aggregation and model performance, as  
621 demonstrated here, and could be useful for informing humanitarian contingency planning for annual rainfall-related  
622 impacts in Nepal and other monsoon-affected countries.

623

#### 624 **6. Conclusions**

625

626 Accounting for the multi-hazard aspects of risk is crucial for disaster risk reduction and humanitarian planning.  
627 Traditional approaches to risk modelling tend to omit the interactions between hazards and, even when these  
628 interactions are accounted for, may struggle to meet the computational demands posed by such complex scenarios.  
629 Here, we demonstrate that a new model based on hypergraph theory, a type of network modelling approach, is able to  
630 efficiently simulate multi-hazard risk. The model framework accounts for the interactions between a driving stimulus  
631 such as an earthquake or rainstorm with processes on the landscape (such as landslides) and exposed infrastructure.  
632 Beyond overcoming computational challenges, this framework can facilitate multi-hazard risk assessments by enabling  
633 the generation of ensembles to explore the importance of different geophysical hazards, larger areas, longer timeframes,  
634 and diverse counterfactual scenarios. This versatility enhances our understanding of complex risk landscapes and  
635 empowers decision-makers with valuable insights for proactive disaster preparedness and response strategies.



636

637 We explore the capabilities of the model through a case study of the 2015  $M_w$  7.8 Gorkha earthquake in Nepal, which  
638 caused widespread damage due to both primary shaking and secondary landslides. We find that the model can reproduce  
639 the overall spatial pattern of earthquake impacts. The observed numbers of completely-damaged buildings in most  
640 districts, including 13 out of the 14 worst-affected districts, fall within the range of model predictions, which depends  
641 primarily on the assumed fragility functions for the typical building types found in Nepal. The model also broadly  
642 reproduces the spatial patterns of structures that were damaged by coseismic landslides in the earthquake, although it  
643 overestimates the absolute number of impacts. This may be due to limitations in the data used by the model to  
644 determine impacts. Importantly, there is an increase in model performance when the results are aggregated over larger  
645 administrative areas; the model does a reasonable job of anticipating the relative impacts at a province or district scale,  
646 but performs much less well at the smaller scales of municipalities or wards. This result suggests that the hypergraph  
647 framework could be usefully applied to rank administrative areas by expected impacts, for example due to a future  
648 earthquake or rainstorm, to underpin pre-disaster contingency planning efforts where large-scale trends are more  
649 important than detailed impact predictions. The computational efficiency of the hypergraph framework, even at the  
650 scale of an entire country such as Nepal, lends itself to the generation of multiple impact scenarios and raises the  
651 possibility of using an ensemble of potential scenario results rather than depending upon single-event scenarios for  
652 disaster preparedness and planning.

653

#### 654 **Author contributions**

655 Funding was acquired by ALD, TRR, and NJR. The study was conceived by ADu, TRR, ALD, and NJR. ADu wrote  
656 the code and carried out the numerical experiments with input from TRR, ALD, NJR, RMR, and MEK. ADu and ALD  
657 prepared the original draft of the manuscript and all authors contributed to review and editing.

658

#### 659 **Competing interests**

660 The authors declare that they have no conflict of interest.

661

#### 662 **Acknowledgements**

663 This research has been supported by the UK Global Challenges Research Fund through the NERC Multi-Hazard and  
664 Systemic Risk programme (grant NE/T01038X/1). The AW3D DEM (©JAXA, RESTEC and NTTDATA) is licensed  
665 via Durham University (UK), with funding from the DFID-UKRI SHEAR programme (project number 201844-112).



## 666 References

667

668 Alvioli, M., Marchesini, I., Reichenbach, P., Rossi, M., Ardizzone, F., Fiorucci, F., and Guzzetti, F.: Automatic  
669 delineation of geomorphological slope units with r.slopeunits v1.0 and their optimization for landslide susceptibility  
670 modelling, *Geoscientific Model Development*, 9, 3975-3991, doi:10.5194/gmd-9-3975-2016, 2016.

671

672 Avouac, J.-P., Meng, L., Wei, S., Wang, T., and Ampuero, J.-P.: Lower edge of locked Main Himalayan Thrust unzipped  
673 by the 2015 Gorkha earthquake, *Nature Geoscience*, 8, 708-711, doi:10.1038/ngeo2518, 2015.

674

675 Bird, J.F., and Bommer, J.J.: Earthquake losses due to ground failure., *Engineering Geology*, 75, 147-179,  
676 doi:10.1016/j.enggeo.2004.05.006, 2004.

677

678 Buzna, L., Peters, K., and Helbing, D.: Modelling the dynamics of disaster spreading in networks, *Physica A: Statistical  
679 Mechanics and Its Applications*, 363, 132-140, doi:10.1016/j.physa.2006.01.059, 2006.

680

681 Chaulagain, H., Gautam, D., and Rodrigues, H.: Revisiting major historical earthquakes in Nepal: Overview of 1833,  
682 1934, 1980, 1988, 2011, and 2015 seismic events, in: *Impacts and Insights of the Gorkha Earthquake*, edited by  
683 Gautam, D., and Rodrigues, H.F.P., Elsevier, pp. 1-17, doi:10.1016/B978-0-12-812808-4.00001-8, 2018.

684

685 Chorley, R.J., and Kennedy, B.A.: *Physical Geography: A Systems Approach*, Prentice-Hall, 1971.

686

687 Croissant, T., Lague, D., Steer, P., and Davy, P.: Rapid post-seismic landslide evacuation boosted by dynamic river  
688 width, *Nature Geoscience*, 10, 680-684, 2017.

689

690 Croissant, T., Steer, P., Lague, D., Davy, P., Jeandet, L., and Hilton, R.G.: Seismic cycles, earthquakes, landslides, and  
691 sediment fluxes: linking tectonics to surface processes using a reduced-complexity model, *Geomorphology*, 339,  
692 87-103, doi:10.1016/j.geomorph.2019.04.017, 2019.

693

694 Daniell, J.E., Schaefer, A.M., and Wenzel, F.: Losses associated with secondary effects in earthquakes, *Frontiers in Built  
695 Environment*, 3, 30, doi:10.3389/fbuil.2017.00030, 2017.

696

697 De Ruiter, M.C., Couasnon, A., Homberg, M.J.C., Daniell, J.E., Gill, J.C., and Ward, P.J.: Why we can no longer ignore  
698 consecutive disasters, *Earth's Future*, 8, doi:10.1029/2019EF001425, 2020.

699

700 Dezső, Z., and Barabási, A.L.: Halting viruses in scale-free networks, *Physical Review E - Statistical, Nonlinear, and  
701 Soft Matter Physics*, 65, 1-4, doi:10.1103/PhysRevE.65.055103, 2002.

702

703 Didier, M., Baumberger, S., Tobler, R., Esposito, S., Ghosh, S., & Stojadinovic, B. (2017). Improving Post-Earthquake  
704 Building Safety Evaluation using the 2015 Gorkha, Nepal, Earthquake Rapid Visual Damage Assessment Data.

705 *Earthquake Spectra*, 33(1\_suppl), 415-438. <https://doi.org/10.1193/112916eqs210m>

706



707 Dorogovtsev, S.N., and Mendes, J.F.F.: Evolution of Networks: From Biological Nets to the Internet and WWW, Oxford  
708 University Press, doi:10.1093/acprof:oso/9780198515906.001.0001, 2003.

709

710 Dunant, A.: Are we missing the target? A bias-variance perspective on multi-hazard risk assessment, *Frontiers in Earth  
711 Science*, 9, 685301, doi:10.3389/feart.2021.685301, 2021.

712

713 Dunant, A., Bebbington, M., and Davies, T.: Probabilistic cascading multi-hazard risk assessment methodology using  
714 graph theory, a New Zealand trial, *International Journal of Disaster Risk Reduction*, 54, 102018,  
715 doi:10.1016/j.ijdrr.2020.102018, 2021a.

716

717 Dunant, A., Bebbington, M., Davies, T., and Horton, P.: Multihazards scenario generator: A network-based simulation  
718 of natural disasters, *Risk Analysis*, 41, 2154-2176, doi:10.1111/risa.13723, 2021b.

719

720 Euler, L.: Solutio problematis ad geometriam situs pertinentis. *Commentarii Academiae Scientiarum Petropolitanae*,  
721 128-140, 1741.

722

723 FEMA: Hazus-MH 2.1 Advanced Engineering Building Module Technical and User's Manual. Federal Emergency  
724 Management Agency,

725 [https://www.fema.gov/sites/default/files/2020-09/fema\\_hazus\\_advanced-engineering-building-module\\_user-manual.pdf](https://www.fema.gov/sites/default/files/2020-09/fema_hazus_advanced-engineering-building-module_user-manual.pdf)

726 , last access 16 April 2024, 2020.

727

728 Gautam, D., Fabbrocino, G., & Santucci de Magistris, F. (2018). Derive empirical fragility functions for Nepali  
729 residential buildings. *Engineering Structures*, 171, 617–628. <https://doi.org/10.1016/j.engstruct.2018.06.018>

730

731 Gill, J.C., Duncan, M., Ciurean, R., Smale, L., Stuparu, D., Schlumberger, J., de Ruyter, M., Tiggeloven, T., Torresan,  
732 S., Gottardo, S., Mysiak, J., Harris, R., Petrescu, E.-C., Girard, T., Khazai, B., Claassen, J., Dai, R., Champion, A.,  
733 Daloz, A. S., ... Ward, P.: Handbook of Multi-hazard, Multi-risk Definitions and Concepts, Zenodo,  
734 <https://doi.org/10.5281/zenodo.7135138>, 2022.

735

736 Gill, J.C., and Malamud, B.D.: Reviewing and visualizing the interactions of natural hazards: Interactions of natural  
737 hazards, *Reviews of Geophysics*, 52, 680-722, doi:10.1002/2013RG000445, 2014.

738

739 Goda, K., Kiyota, T., Pokhrel, R.M., Chiaro, G., Katagiri, T., Sharma, K., and Wilkinson, S.: The 2015 Gorkha Nepal  
740 earthquake: Insights from earthquake damage survey, *Frontiers in Built Environment*, 1, doi:10.3389/fbuil.2015.00008,  
741 2015.

742

743 Government of Nepal - National Planning Commission. (2015). *Nepal Earthquake 2015 Post Disaster Needs  
744 Assessment* Vol. A: Key Findings.

745 <https://www.worldbank.org/content/dam/Worldbank/document/SAR/nepal/PDNA%20Volume%20>

746 [A%20Final.pdf](https://www.worldbank.org/content/dam/Worldbank/document/SAR/nepal/PDNA%20Volume%20)

747



748 Government Office for Science: Government Office for Science Annual Review 2012-2013,  
749 <https://assets.publishing.service.gov.uk/media/5a7cca70ed915d63cc65cdd6/13-p95-government-office-for-science-annual-review-2012-2013.pdf>, 2012.  
750  
751  
752 Guragain, R., Shrestha, S. N., Pradhan, S., & Meguro, K. (2020). NUMERICALLY DEVELOPPED AND FIELD  
753 OBSERVED SEISMIC FRAGILITY FUNCTIONS FOR NEPALESE BUILDINGS.  
754  
755 Hearn, G.J., and Shakya, N.M.: Engineering challenges for sustainable road access in the Himalayas, Quarterly Journal  
756 of Engineering Geology and Hydrogeology, 50, 69-80, doi:10.1144/qjgegh2016-109, 2017.  
757  
758 Hochrainer-Stigler, S., Trogrlić, R. Š., Reiter, K., Ward, P.J., de Ruiter, M.C., Duncan, M J., Torresan, S., Ciurean, R.,  
759 Mysiak, J., and Stuparu, D.: Toward a framework for systemic multi-hazard and multi-risk assessment and  
760 management, iScience, 26, 106736, doi:10.1016/j.isci.2023.106736, 2023.  
761  
762 Hou, A.Y., Kakar, R.K., Neeck, S., Azarbarzin, A.A., Kummerow, C.D., Kojima, M., Oki, R., Nakamura, K., and  
763 Iguchi, T.: The Global Precipitation Measurement Mission, Bulletin of the American Meteorological Society, 95(5),  
764 701-722, doi:10.1175/BAMS-D-13-00164.1, 2014.  
765  
766 Jimée, G.K., Meguro, K., & Dixit, A.M.: Nepal, a multi-hazard risk country: Spatio-temporal analysis, Journal of Nepal  
767 Geological Society, 58, 145-152, doi:10.3126/jngs.v58i0.24599, 2019.  
768  
769 Kappes, M.S., Keiler, M., von Elverfeldt, K., and Glade, T.: Challenges of analyzing multi-hazard risk: A review,  
770 Natural Hazards, 64, 1925-1958, doi:10.1007/s11069-012-0294-2, 2012.  
771  
772 Kargel, J.S., Leonard, G.J., Shugar, D.H., Haritashya, U.K., Bevington, A., Fielding, E., Fujita, K., Geertsema, M.,  
773 Miles, E., ... and Steiner, J.: Geomorphic and geologic controls of geohazards induced by Nepal's 2015 Gorkha  
774 earthquake, Science, 351, doi:10.1126/science.aac8353, 2016.  
775  
776 Kincey, M.E., Rosser, N.J., Robinson, T.R., Densmore, A.L., Shrestha, R., Pujara, D.S., Oven, K.J., Williams, J.G., and  
777 Swirad, Z.M.: Evolution of coseismic and post-seismic landsliding after the 2015  $M_w$  7.8 Gorkha earthquake, Nepal,  
778 Journal of Geophysical Research – Earth Surface, 126, doi:10.1029/2020JF005803, 2021.  
779  
780 Kincey, M.E., Rosser, N.J., Densmore, A.L., Robinson, T.R., Shrestha, R., Singh Pujara, D., Horton, P., Swirad, Z.M.,  
781 Oven, K.J., and Arrell, K.: Modelling post-earthquake cascading hazards: changing patterns of landslide runout  
782 following the 2015 Gorkha earthquake, Nepal, Earth Surface Processes and Landforms, 48, 537-554,  
783 doi:10.1002/esp.5501, 2022.  
784  
785 Lallemand, D., Soden, R., Rubinyi, S., Loos, S., Barns, K., & Bhattacharjee, G. (2017). Post-Disaster Damage  
786 Assessments as Catalysts for Recovery: A Look at Assessments Conducted in the Wake of the 2015 Gorkha, Nepal,  
787 Earthquake. *Earthquake Spectra*, 33(1\_suppl), 435–451. <https://doi.org/10.1193/120316eqs222m>  
788



- 789 Luo, H.Y., Zhang, L.M., Zhang, L.L., He, J., and Yin, K.S.: Vulnerability of buildings to landslides: the state of the art  
790 and future needs, *Earth-Science Reviews*, 238, 104329, doi:10.1016/j.earscirev.2023.104329, 2023.
- 791
- 792 Marano, K.D., Wald, D.J., and Allen, T.I.: Global earthquake casualties due to secondary effects: a quantitative analysis  
793 for improving rapid loss analyses, *Natural Hazards*, 52, 319-328, doi:10.1007/s11069-009-9372-5, 2010.
- 794
- 795 Mignan, A., Wiemer, S., & Giardini, D.: The quantification of low-probability-high-consequences events: Part I. A  
796 generic multi-risk approach, *Natural Hazards*, 73, 1999-2022, doi:10.1007/s11069-014-1178-4, 2014.
- 797
- 798 McAdoo, B.G., Quak, M., Gnyawali, K.R., Adhikari, B.R., Devkota, S., Rajbhandari, P.L., and Sudmeier-Rieux, K.:  
799 Roads and landslides in Nepal: how development affects environmental risk, *Natural Hazards and Earth System  
800 Science*, 18, 3203-3210, doi:10.5194/nhess-18-3203-2018, 2018.
- 801
- 802 Milledge, D.G., Densmore, A.L., Bellugi, D., Rosser, N.J., Watt, J., Li, G., and Oven, K.J.: Simple rules to minimise  
803 exposure to coseismic landslide hazard, *Natural Hazards and Earth System Sciences*, 19, 837-856,  
804 doi:10.5194/nhess-19-837-2019, 2019.
- 805
- 806 Ming, X., Liang, Q., Dawson, R., Xia, X., and Hou, J.: A quantitative multi-hazard risk assessment framework for  
807 compound flooding considering hazard inter-dependencies and interactions, *Journal of Hydrology*, 607, 127477,  
808 doi:10.1016/j.jhydrol.2022.127477, 2022.
- 809
- 810 Reichenbach, P., Rossi, M., Malamud, B. D., Mihir, M., and Guzzetti, F.: A review of statistically-based landslide  
811 susceptibility models, *Earth-Science Reviews*, 180, 60-91, doi:10.1016/j.earscirev.2018.03.001, 2018.
- 812
- 813 Roback, K., Clark, M.K., West, A.J., Zekkos, D., Li, G., Gallen, S.F., Chamlagain, D., and Godt, J. W.: The size,  
814 distribution, and mobility of landslides caused by the 2015  $M_w$  7.8 Gorkha earthquake, Nepal, *Geomorphology*, 301,  
815 121-138, doi:10.1016/j.geomorph.2017.01.030, 2018.
- 816
- 817 Robinson, T.R., Rosser, N.J., Densmore, A.L., Oven, K.J., Shrestha, S.N., and Guragain, R.: Use of scenario ensembles  
818 for deriving seismic risk, *Proceedings of the National Academy of Sciences*, 115, E9532-E9541,  
819 doi:10.1073/pnas.1807433115, 2018.
- 820
- 821 Rosser, N., Kinsey, M., Oven, K., Densmore, A., Robinson, T., Pujara, D. S., Shrestha, R., Smutny, J., Gurung, K.,  
822 Lama, S., and Dhital, M.R.: Changing significance of landslide hazard and risk after the 2015  $M_w$  7.8 Gorkha, Nepal  
823 earthquake, *Progress in Disaster Science*, 10, 100159, doi:10.1016/j.pdisas.2021.100159, 2021.
- 824
- 825 Sylvester, J.J.: On an application of the new atomic theory to the graphical representation of the invariants and  
826 covariants of binary quantics, with three appendices, *American Journal of Mathematics*, 1, 64-104, 1878.
- 827
- 828 Terzi, S., Torresan, S., Schneiderbauer, S., Critto, A., Zebisch, M., and Marcomini, A.: Multi-risk assessment in  
829 mountain regions: A review of modelling approaches for climate change adaptation, *Journal of Environmental  
830 Management*, 232, 759-771, doi:10.1016/j.jenvman.2018.11.100, 2019.



831

832 Tian, Y., Owen, L.A., Xu, C., Ma, S., Li, K., Xu, X., Figueiredo, P.M., Kang, W., Guo, P., Wang, S., Liang, X., and  
833 Maharjan, S.B.: Landslide development within three years after the 2015  $M_w$  7.8 Gorkha earthquake, Nepal, *Landslides*,  
834 17, 1251-1267, doi:10.1007/s10346-020-01366-x, 2020.

835

836 Tilloy, A., Malamud, B.D., Winter, H., and Joly-Laugel, A.: A review of quantification methodologies for multi-hazard  
837 interrelationships, *Earth-Science Reviews*, 196, 102881, doi:10.1016/j.earscirev.2019.102881, 2019.

838

839 UNISDR: Hyogo Framework for Action 2005-2015: Building the resilience of nations and communities to disasters, in:  
840 Extract from the Final Report of the World Conference on Disaster Reduction (A/CONF. 206/6), 380, Geneva: The  
841 United Nations International Strategy for Disaster Reduction, 2005.

842

843 UNISDR: Report of the Open-ended Intergovernmental Expert Working Group on Indicators and Terminology Relating  
844 to Disaster Risk Reduction, [https://www.preventionweb.net/files/50683\\_oiewgreportenglish.pdf](https://www.preventionweb.net/files/50683_oiewgreportenglish.pdf), 2016.

845

846 Ward, P.J., Blauhut, V., Bloemendaal, N., Daniell, J.E., de Ruiter, M.C., Duncan, M.J., Emberson, R., Jenkins, S.F.,  
847 Kirschbaum, D., Kunz, M., Mohr, S., Muis, S., Riddell, G.A., Schäfer, A., Stanley, T., Veldkamp, T.I.E., and  
848 Winsemius, H.C.: Review article: Natural hazard risk assessments at the global scale, *Natural Hazards and Earth  
849 System Sciences*, 20, 1069-1096, doi:10.5194/nhess-20-1069-2020, 2020.

850

851 Ward, P.J., Daniell, J., Duncan, M., Dunne, A., Hananel, C., Hochrainer-Stigler, S., Tijssen, A., Torresan, S., Ciurean,  
852 R., Gill, J.C., Sillmann, J., Couasnon, A., Koks, E., Padrón-Fumero, N., Tatman, S., Tronstad Lund, M., Adesiyun, A.,  
853 Aerts, J.C.J.H., Alabaster, A., ... and de Ruiter, M.C.: Invited perspectives: A research agenda towards disaster risk  
854 management pathways in multi-(hazard-)risk assessment, *Natural Hazards and Earth System Sciences*, 22, 1487-1497,  
855 doi:10.5194/nhess-22-1487-2022, 2022.

856

857 Williams, J.G., Rosser, N.J., Kinsey, M.E., Benjamin, J., Oven, K.J., Densmore, A.L., Milledge, D.G., Robinson, T.R.,  
858 Jordan, C.A., and Dijkstra, T.A.: Satellite-based emergency mapping: landslides triggered by the 2015 Nepal  
859 earthquake, *Natural Hazards and Earth System Sciences*, 18, 185-205, doi:10.5194/nhess-18-185-2018, 2018.

860

861 Wolf, M.M., Klinvex, A.M., and Dunlavy, D.M.: Advantages to modeling relational data using hypergraphs versus  
862 graphs, *IEEE High Performance Extreme Computing Conference (HPEC)*, 1-7, doi:10.1109/HPEC.2016.7761624,  
863 2016.

864

865 Woodard, J.B., Mirus, B.B., Wood, N.J., Allstadt, K.E., Leshchinsky, B.A., and Crawford, M.M. (2024). Slope Unit  
866 Maker (SUMak): An efficient and parameter-free algorithm for delineating slope units to improve landslide modelling,  
867 *Natural Hazards and Earth System Sciences*, 24, 1-12, doi:10.5194/nhess-24-1-2024, 2024.

868

869 Zschau, J.: Where are we with multihazards, multirisks assessment capacities? in: *Science for Disaster Risk  
870 Management 2017: Knowing Better and Losing Less*, edited by: Poljanšek, K., Marín Ferrer, M., De Groeve, T., and  
871 Clark, I., EUR 28034 EN, Publications Office of the European Union, Luxembourg, doi:10.2788/688605, JRC102482,  
872 2017.